www.czasopisma.pan.pl PAN POLSKA AKADEMIA NAUK www.journals.pan.pl

Arch. Metall. Mater. **66** (2021), 2, 581-591

DOI: 10.24425/amm.2021.135895

Y. GARIP[1*], Z. GARIP[2], O. OZDEMIR[1]

APPLICATION OF ARTIFICIAL NEURAL NETWORK FOR PREDICTION OF THE CYCLIC OXIDATION BEHAVIOR OF ELECTRICAL RESISTANCE SINTERED GAMMA-TiAl INTERMETALLICS

TiAl based intermetallics are widely used for structural applications in aviation, chemical engineering, automotive and sports equipment. In this study, the electrical resistance sintering (ERS) technology used in the production of gamma-TiAl intermetallics is based on the principle of applying pressure simultaneously with a high-density electric current. The purpose of this study was to investigate the cyclic oxidation resistance of Ti-44Al-3Mo and Ti-44Al-3Nb alloys (at.%) and the applicability of artificial neural network (ANN) modeling for the forecast of the oxidation behavior of these alloys. In order to obtain this aim, the alloys sintered by ERS were oxidized at 900°C for 360 h and then the oxidation behaviors of them are evaluated by plotting a graph between weight change as a function of time. The data collected after the oxidation experiments were used to construct the prediction models. The modelling results show that a good agreement between experimental results and prediction results was found. The oxidized alloys were characterized using XRD and SEM-EDS. The XRD patterns revealed the oxidation products are composed of TiO_2 and Al_2O_3 oxides. SEM-EDS analysis indicated that the oxide scales of alloys are made up of a multilayered structure.

Keywords: TiAl, Artificial neural networks, Oxidation kinetics, Electrical resistance sintering, Aluminides

1. Introduction

Intermetallics are defined as solid phases consisting of two or more metallic or semi-metallic elements with an ordered structure and generally well-defined and a fixed stoichiometry [1]. One of these compounds, based on titanium aluminide intermetallic, has drawn attention as a material for high-temperature applications due to a combination of outstanding properties such as high melting point, low density, adequate high specific strength, creep resistance and elastic modulus as well as good oxidation and corrosion resistance [2-5]. In addition, these materials have better thermal conductivity compared to ceramics and offer ductility while maintaining their structural stability under service conditions [6]. The outstanding advantages of these intermetallic compounds make them extremely promising for the automotive and aerospace industries [7]. However, apart from mentioned excellent properties, TiAl alloys possess poor ductility and fracture toughness at room temperature and lack of hot deformability [2], inadequate oxidation resistance at temperatures above 800°C [8], difficult and high-cost manufacture [9].

Most alloys exposed to high temperatures are inevitably oxidized. Maintenance and repair costs resulting from oxidation of these materials trouble the industrial companies economically. Therefore, researching the oxidation behavior of TiAl alloys in service conditions has always been important for scientists and engineers. Moreover, the improvement in the oxidation resistance of these alloys at high temperatures contributes significantly to the industrialization of other high-temperature applications, especially in the aviation field.

In order to improve the high temperature oxidation performance of TiAl alloys, different modification methods such as adding alloying elements and coating systems have been adopted [2,8,10,11]. The approach of modifying the chemical composition of TiAl alloys with the addition of alloy elements is a simple and highly effective method [10]. Many investigations have been done concerning the oxidation behavior of ternary or quaternary alloying elements added TiAl alloys and Mo, W and Nb elements have been reported to enhance the high temperature oxidation behavior of TiAl alloys [4,12-15].

The positive effects of these elements can be explained by considering various factors: when an alloying element with a higher valence than that of Ti is incorporated in the scale, oxygen vacancy concentration in the TiO_2 lattice decreases via a mechanism called doping effect in accordance with the

[1] SAKARYA APPLIED SCIENCE UNIVERSITY, TECHNOLOGY FACULTY, DEPARTMENT OF METALLURGY AND MATERIALS ENGINEERING, ESENTEPE CAMPUS, 54187, SAKARYA-TURKEY
[2] SAKARYA APPLIED SCIENCE UNIVERSITY, TECHNOLOGY FACULTY, DEPARTMENT OF COMPUTER ENGINEERING, ESENTEPE CAMPUS, 54187, SAKARYA-TURKEY
* Corresponding author: yigitgarip@hotmail.com

principle of maintaining the electroneutrality [4], decrease of O diffusion and solubility in the substrate resulting in enhanced scale-substrate adherence [12], As a result of increasing Al activity, the formation of the protective Al_2O_3 layer can be supported on the alloy surface. As far as mechanical characteristics are concerned, it is worth mentioning that the addition of Nb and Ta alloying elements decrease the creep rate as they are slower diffusers in the TiAl alloys [16].

The production of a TiAl intermetallic can be a discouraging task, due to the high qualities expected from the alloy, in terms of high-temperature and mechanical properties. Therefore, scientists and engineers are faced with the fact of finding alternative processes to conventional methods to produce TiAl based alloys. Under these circumstances, it can be regarded that the powder metallurgy route can be used as an alternative in the production of the mentioned materials. The powder metallurgy technology offers the preparation of material with superior mechanical properties, faster preparation process, material with good dimensional stability, ease of reproducibility, lesser human contact and minimum inherent defects [17]. In the light of these developments, electrical resistance sintering (ERS) technique brings many advantages compared to traditional sintering processes in powder metallurgy. These include the shorter sintering time, sintered parts with net or near-net shapes, the application of lower loads to obtain higher densification rates, higher heating rates and prevention of excessive grain growth [4,5,18]. It is worth mentioning here that the high heating rate provided by this method makes the use of the protective atmosphere unnecessary during sintering [4,5]. Moreover, shorter processing times in engineering applications often play an important role in productivity growth. Regarding the main drawbacks of ERS process, it can be said that the difficulty of achieving a uniform heat distribution inside the compact during operation and the absence of sufficient theoretical knowledge of the existence of various mechanisms [18]. However, applications involving hard-to-produce materials such as hard metals, nanocomposites, amorphous or nanocrystalline structures and refractory materials have contributed to the rapid increase of interest in ERS technology in the last 30 years [18].

Computational modeling can be regarded as a highly effective approach in modeling complex experimental data. Artificial neural networks (ANN), one of the most efficient modern modeling techniques, has gained considerable attention in material science in recent years as it can map input-output relationships using a statistical approach as well as having ease of application and generalization ability [19-22]. ANN system was applied successfully by many researchers with the aim of modeling the oxidation [19,23] and corrosion [24] behavior of various materials, optimization of the effect of thermomechanical treatments [25], design of casting alloy composition [26], prediction of mechanical properties [20,27] and microstructure modeling [28]. However, based on open literature, studies on the modeling of the cyclic oxidation behavior of TiAl alloys using artificial neural network (ANN) are scarce.

The present study aims to investigate the cyclic oxidation behavior of at.% Ti-44Al-3Mo and Ti-44Al-3Nb alloys sintered by electrical resistance sintering (ERS) technique. After 360 hours of oxidation at 900°C, in order to predict oxidation behavior of the alloys, the database of the weight changes experienced by the alloys was modelled by using Artificial Neural Network (ANN) approach. Additionally, the obtained results in this study present an opportunity to ensure reference in the investigation of the oxidation properties of TiAl alloys.

2. Experimental procedure

2.1. Powder preparation and sintering

Titanium aluminides used in this study have the nominal composition of (at.%) Ti-44Al-3Mo and Ti-44Al-3Nb (hereafter denoted as TiAlMo and TiAlNb, respectively) were sintered by electrical resistance sintering (ERS) technique. The used elemental powders were composed of titanium (purity 99.5%, 40 µm), aluminum (purity 99.5%, 7-15 µm), molybdenum (purity 99.6%, 3-7 µm) and niobium (purity 99.8%, 40 µm).

The powders were weighed according to the nominal compositions. The mechanical mixer was used to obtain a homogenous powder mixture for a period of 6 hours at a rotation speed of 165 r/min. in a dry environment. The mixed powders of 5 g were discharged into a steel die with an inner diameter of 20 mm and an outer diameter of 50 mm. Afterward, the powder mass to be sintered is placed between two counter-sliding punches. The ERS parameters are as follows; uniaxial applied pressure was 100 MPa, current intensity 4500 amperes and holding time was 25 minutes in air. The electric current applied simultaneously with a uniaxial mechanical load was maintained at the set value throughout ERS process. The sintering activities were monitored by the controller during the process. At the completion of sintering, the sintered sample was taken from the die using uniaxial load and was allowed to cool down to ambient temperature. Finally, the sintered sample with Ø 20 mm diameter and 5 mm thickness was obtained.

2.2. Oxidation testing

Before the oxidation test, the original surface area of each samples was identified using the Solidworks and then weighed by a digital balance with an accuracy of 0.01 mg. The oxidation testing was carried out in an electric resistance furnace at 900°C for 360 hours and 30 cycles. A cycle involves heating the samples to the test temperature and holding them in the furnace for 12 h. At the end of the cycle, the samples were removed from the furnace and then air cooled in room temperature. Afterward, the samples were again weighed to evaluate the oxidation kinetic. The weight measurements were repeated for each cycle. In addition, the three measurements were done for each sample in the cycle. Then, the obtained data were averaged and recorded. This procedure was reapplied for each oxidation cycle.

2.3. Sample characterization

In order to perform the SEM studies, the sintered samples were gradually grounded by SiC papers up to 1200 and subsequently polished using 1 μm diamond particles. The samples were etched by a Kroll reagent: 3 vol.% HF, 5 vol.% HNO_3, 92 vol.% distilled water.

X-ray diffraction analysis (Rigaku, D/MAX-B/2200/PC) was used to identify the phase constitution of the samples and oxidation products using diffractometer with Cu Kα radiation and operated at 40 kV and 40 mA. The XRD data scanning angle 2θ ranges from 20° to 90° with a step size of 0.02°. The initial microstructures of the samples, the surface morphology and the cross-sectional microstructure of the oxidized samples were observed by a scanning electron microscopy (SEM, JEOL JSM-6060, LV). Chemical compositions of the present phases were examined by energy-dispersive spectroscopy (EDS, IXRF 5000). Three EDS analyses were performed for each phase area and the average of these measurements was reflected in the graph. The relative densities of the samples were calculated by Archimedes' principle, based on the immersion technique in distilled water. The microhardness of the samples was determined using Vickers diamond indenter. For each sample, 4 measurements were conducted using the application of a 200 g load for a 10 sec and measurements were averaged.

3. Artificial neural network modelling

Artificial neural networks are often used to model various complex and nonlinear processes. The ANN model has superior features such as learning and generalization capability, high parallelism, working with an unlimited number of variables [25]. In addition, derivatives of the artificial neural network have been developed thanks to many important components such as training algorithms, different types of activation function, pre- and post-processing, error functions, the weights initialization and the training data collection [29].

ANN is generally of two approaches: static and dynamic network. In static networks such as Radial Basis, Multilayer perceptron (MLP), Learning Vector Quantization and Kohonen adaptive Neuro-Fuzzy Inference Systems, output nodes are linked directly to the input nodes. There is also no feedback from the output nodes to the input and the order of the incoming data is not important [30]. In dynamic networks such as the distributed time delay network, the nonlinear autoregressive network (NARX), the focused time delay network (FTDN) and the Layer-Recurrent Network of Elman network, the output nodes depend on the current and previous data of the input and output nodes and the network structure [24].

ANN has a complex network structure consisting of different layers [25]. Artificial neural networks (ANN) with prediction and simulation capabilities model a problem as an input node, hidden layer and output node [24,30]. The number of hidden layers determines the complexity of the neural networks. Adjusting the number of hidden layers correctly improves the accuracy of the artificial neural network, if not, data from the system may be invalid. Therefore, before modeling a problem, the number of hidden layers must be determined in a way to provide optimum results [19].

In the study, nonlinear autoregressive neural network (NARX) method, which is one of the dynamic networks, was used to estimate the oxidation behavior of alloys.

3.1. Non-linear Autoregressive Neural Network (NARX)

NARX is a recurrent neural network method for nonlinear dynamic systems using a given input and output as data. Moreover, it provides the response of the current data to be identified as a function of past data of the output [31]. NARX models accept discrete and continuous dynamic inputs. They also have both open-loop and closed-loop operating performance, and this performance has been greatly improved in long-term problems [32]. The NARX model not only uses the current and previous values of the input data to find the estimated output of the network, but also gives feedback based on the current and previous values of the output data [24]. The function of the basic structure of the NARX model is shown in Equation 1. Two hidden layer NARX models used to predict weight change are presented in Figure 1.

$$y[t+1] = f\begin{pmatrix} y[t], y[t-1], .., y[t-n_y], \\ x[t], x[t-1], \ldots, x[t-n_x] \end{pmatrix} \quad (1)$$

n_y and n_x in Equation 1 are the values used in the time delay of the output and input data, respectively.

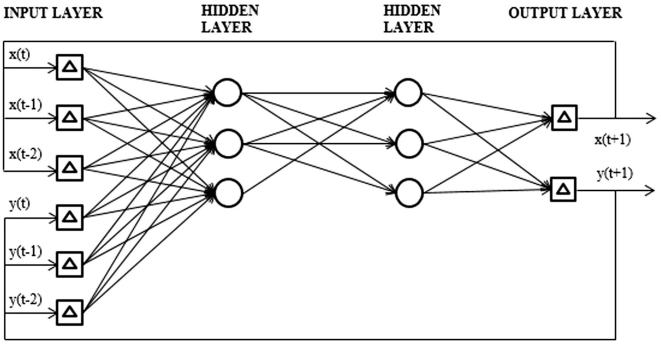

Fig. 1. Schematic diagram of two-layer NARX neural network model

In order to test the accuracy of the model, the mean squared error (*MSE*) is calculated according to the variance of the target signal [32]. The *MSE* function is expressed in Equation 2 where t_i is the target output data, a_i is the output data of the artificial neural network, and N is the number of samples.

$$MSE = \frac{1}{N}\sum_{i=1}^{N}(e_i)^2 = \frac{1}{N}\sum_{i=1}^{N}(t_i - a_i)^2 \quad (2)$$

3.2. Proposed ANN model

While the input data of the ANN model is oxidation time, the data obtained from the output is the weight change of the alloys.

The input is oxidation time and the output is the weight change of the oxidized alloys. This oxidation time information was given to ANN in NARX structure and weight changes were obtained. This structure was developed using Matlab Artificial Neural Network Toolbox. The first hidden layer of the NARX model is defined as 20 neurons, the second hidden layer is 10 neurons and the output layer is 2 neurons. The entire values are divided into three sets (80% for training data, 10% for testing data and 10% validation data). Levenberg-Marquardt back propagation algorithm was chosen to train the ANN. In the feedback, 2 units of delay are added to each oxidation time signal with a position signal.

4. Results and discussion

4.1. Characterization of the produced alloys

The morphologies of the powders used as starting material are shown in Fig. 2. It can be clearly discerned that the particles of Nb and Ti are sharp-edged while Mo and Al particles have a spherical shape. However, it was observed that some Mo particles are agglomerated.

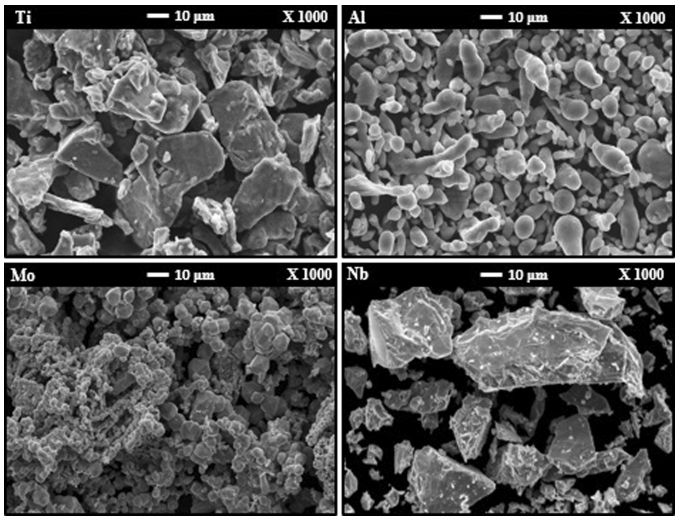

Fig. 2. SEM images of used in this study elemental powders

In the binary Ti-Al binary phase diagram [33], four different intermetallic phases exist, namely α_2-Ti_3Al, γ-TiAl, $TiAl_2$ and $TiAl_3$ [33]. Particularly, dual phase ($\alpha_2 + \gamma$) based TiAl alloys have attracted the attention of researchers for many years due to their satisfactory properties [2]. According to the Ti-Al binary phase diagram, TiAl alloy with the composition of at.% 44 Al solidifies from the single-phase region of the α during the cooling as follows: $\alpha \rightarrow \alpha + \gamma \rightarrow \alpha_2 + \gamma$.

XRD patterns show that the alloys are consisted of α_2-Ti_3Al and γ-TiAl phases (Fig. 3). During sintering, $TiAl_3$ intermediate phase, which has a lower free energy compared to both phases, is formed [4].

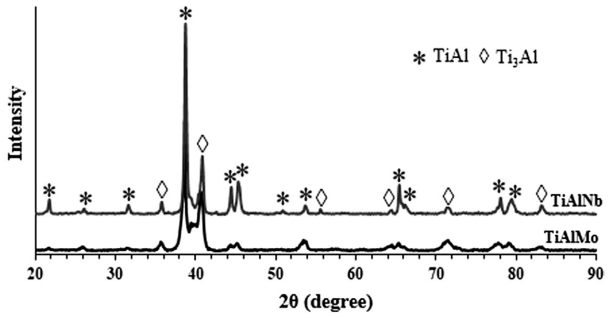

Fig. 3. XRD patterns of the alloys produced by ERS

The SEM images of the ERSed alloys and the chemical compositions corresponding to the points are shown in Figure 4 and Table 1, respectively. SEM images of the TiAlMo and TiAlNb alloys showed that the microstructures were composed of three different phase areas as gray tone, dark-gray tone and bright phase. From the EDS analysis results (Table 1), the chemical composition of the dark area (points 1 and 4) corresponds to γ-TiAl phase and that of the gray area (points 2 and 5) corresponds to α_2-Ti_3Al phase. As shown in the Ti-Al system, the Ti_3Al phase exists between at.% 37-49 Al content, while the TiAl phase exists between at.% 48.5-66 Al content [34]. The bright regions (points 3 and 6) surrounded by gray areas can be seen on the microstructure of the alloys. EDS point analysis shows that Mo and Nb are present in a high amount at points 3 and 6, respectively. However, as shown in Table 1, the chemical composition of these points was near to the theoretical one. It seems that these Mo and Nb elements need longer processing time to

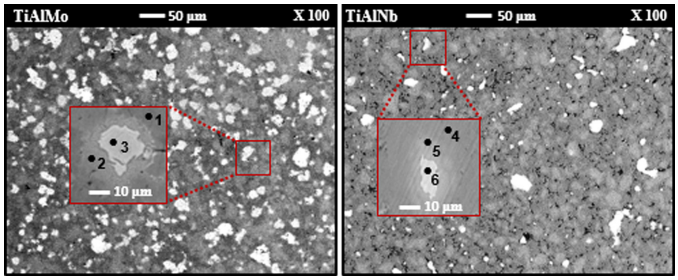

Fig. 4. SEM images of the microstructures of alloys

TABLE 1

Chemical compositions (at.%) of points shown in Fig. 7

Point	Ti	Al	Mo	Nb
1	44.3	55.1	0.6	—
2	63.8	34.8	1.4	—
3	49.9	42.6	7.5	—
4	46.6	52.6	—	0.8
5	72.2	26.2	—	1.6
6	45.2	46.7	—	8.1

be fully dissolved in the TiAl. In a work on the microstructure evolution of TiAl, Lagos and Agote [35] sintered Ti-48Al-2Cr-2Nb (at.%) alloy by means of SPS at 650°C, 700°C, 1100°C and 1300°C and they reported that the diffusion of Nb was not complete even at 1300°C for 8 min. According to their XRD results, the microstructure of the alloy is constituted of the γ and α_2 phases, similar to that observed in this work.

The density properties of the alloys calculated according to the Archimedes' principle are listed in Table 2. Since the density depends on the chemical composition, the densities of γ-TiAl and α_2-Ti_3Al phases are varying between 3.7-3.9 and 4.1-4.7 g cm^{-3}, respectively [4]. The microstructures of alloys were made up of γ-TiAl and α_2-Ti_3Al phases and thus can be expected that the experimental densities were also in the range of the density values of the mentioned two phases. It can be noticed that the relative density of TiAlMo alloy was slightly higher in comparison to the TiAlNb alloy.

TABLE 2

Density properties of the alloys

Alloy	Experimental density (g cm^{-3})	Theoretical density (g cm^{-3})	Relative density (%)
TiAlMo	4.324±0.003	4.375	98.8
TiAlNb	4.180±0.002	4.248	98.4

Regarding the use of powder metallurgy based routes in the production of TiAl alloys, the great difference between the diffusion rate of the Ti and Al atoms brings about the Kirkendall effect [4]. When the pressure is not applied during sintering, surface cracking and swelling may take place in the alloy as a result of the formation of Kirkendall pores [36]. It is important to note that no surface cracking or swelling occurs on the ERS process since current and pressure are applied simultaneously. Besides, the pressure used in this system improves the consolidation by generating plastic deformation that shrinks the pores. Thus, one-step sintering procedure can obtain the parts with high density. The microhardness of the TiAlMo and TiAlNb alloys are found to be 441±24 and 457±19 $Hv_{0.2}$, respectively.

4.2. Oxidation weight change analysis

Cyclic oxidation behaviors of the alloys are characterized by their weight change as a function of oxidation cycles. The weight change per unit area was calculated by dividing the weight difference of the alloy weighed before and after oxidation test ($m_2 - m_1$) with the surface area. The weight change per unit area can be considered as the total of the weight gain due to the formation of oxides and the weight loss due to the spallation of oxide scale or volatilization of gas species. The cyclic oxidation kinetics of the alloys were determined by the following equation:

$$\Delta W = \frac{(m_2 - m_1)}{A} \tag{3}$$

where ΔW presents the weight change per unit area (mg/cm^2), m_1 presents the initial weight (mg), m_2 present the weight after each cycle (mg), and A presents the total surface area of the sample (cm^2).

Figure 5 shows the weight change curves of the TiAlMo and TiAlNb alloys obtained during cyclic oxidation. It can be clearly seen that the oxidation behavior of both alloys exposed to oxidation for 360 hours at 900°C is similar. In the first 24 hours of oxidation testing, a significant weight increase can be seen as a result of rapid oxidation of alloys. This phenomenon is called the incubation stage [2]. It can be said that the oxidation process is controlled by the formation of oxidation products at this incubation stage. Regarding the processes occur in the incubation stage, adsorption and absorption of oxygen by the alloy surface occurs. Moreover, as a result of the alloy components (Ti and Al) have high oxidation activity, it is considered that the nucleation and growth of oxides at the TiAl surface form easily. Additionally, the unoxidized surface can support the initiation of oxidation reactions. According to the curves in Fig. 5, the weight change per unit area decreases as the oxidation progresses with time. This result can be tackled by considering two approaches, the first is that a rich Al_2O_3 layer may have developed in the scale, the other is the diffusion distance of anions and cations increases because of the increase in scale thickness. The latter consideration is concerning the nature of parabolic oxidation kinetics, i.e. the weight change per unit area is initially high but decreases with time. At the 228th hour of oxidation, the TiAlMo and TiAlNb alloys experienced similar oxidation behavior resulting in the weight change of 7.1 and 7.2 mg/cm^2, respectively. After that, the oxidation rate of TiAlNb tended to decrease compared to TiAlMo. The final weight changes of the TiAlMo and TiAlNb were about 8.3 and 7.55 mg/cm^2, respectively.

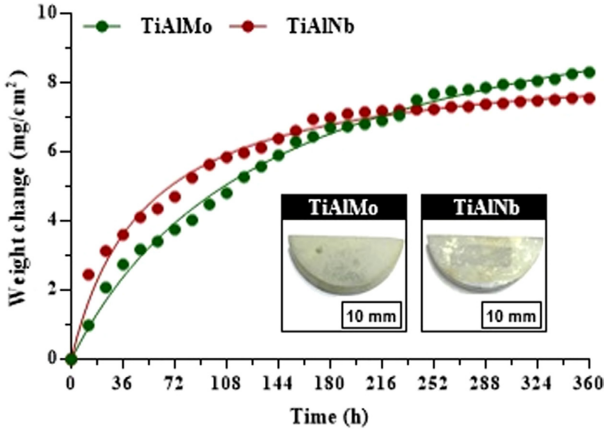

Fig. 5. The variation of weight change with respect to oxidation time for TiAl alloys. Insets show the macro photos of the alloys after oxidation at 900°C for 360 hours

It is worth mentioning that the TiAl parts are currently used in low-pressure stages of aero turbines and the turbocharger of car engines operating at temperatures not exceeding 750°C and 850°C, respectively [37]. Cyclic oxidation test creates more challenging conditions on materials than isothermal test. TiAl

components in the gas turbine engine are heated very quickly from room temperature to service temperature during the engine activation. Therefore, these materials are not only exposed to high temperatures but also thermal shocks because of the periodical heating and cooling process. It is important to note that the occurred spallation in both alloys is a negligible amount. The oxide scales of the TiAlMo and TiAlNb alloys showed good adherence to the substrate.

As far as the effects of alloying elements are concerned, it can be surely said that the additions of Mo and Nb enhance the oxidation resistance of the studied alloys. According to the results obtained from our previous study [4], the final weight change of the Ti-48Al (at.%) alloy subjected to the same experimental conditions was about 42 mg/cm^2 after 180 hours of oxidation at 900°C. However, although the alloys designed for this study have less Al content (at.% 44), the final weight change after 360 hours of oxidation is much less, as stated earlier, thanks to the 3Mo and 3Nb (at.%) additions. The results obtained concerning Mo addition in this study are in good agreement with the one reported by Anada and Shida [38] who studied the role of the Mo addition on the oxidation resistance of Ti-48Al (at.) and observed that the ΔW reduced with the increase of Mo content (up to at.% 2.4). The beneficial effect extent of alloying elements to oxidation resistance followed the order: Mo > Nb > Si [37]. Other points to be mentioned about the effects of Mo and Nb alloy elements on the oxidation resistance of TiAl alloys are that MoO_3 can cause small porosities on the surface as a result of evaporation above 700°C [39] and the addition of high amounts of Nb can reduce the oxidation resistance of TiAl alloys due to the formation of Nb_2O_5 [40].

The data of weight change per unit area (ΔW) of the alloys versus oxidation time (t) have been analyzed to obtain the kinetic parameters such as oxidation rate constant (k_n) and oxidation rate exponent (n). A power law equation is used as follows [41]:

$$(\Delta W)^n = k_n t \tag{4}$$

Taking the logarithm of Equation 4 as follows:

$$\text{In}\,(\Delta W) = (1/n)\,\text{In}\,k + (1/n)\,\text{In}\,t \tag{5}$$

Thus, the values of n can be determined by analysis of the slope of the best fit line for a double logarithm plot of the weight change per unit surface area against oxidation time. The oxidation rate exponent is based on the function n =1/m, which is the reverse of the slope determined from the linear regression in Fig. 6(a). The relationship between the n value and oxidation kinetics can be described as follows: n = 1, 2, 3 correspond to linear, parabolic and cubic kinetics, respectively.

According to the obtained n values in Table 3, it can be said that the oxidation kinetics of the TiAlMo obeys a nearly parabolic relationship, while that of the TiAlNb follows a rate law intermediate between parabolic and cubic relationship. The slope of the straight line in the graph of $(\Delta W)^n$ versus time plotted using the n values is equal to the oxidation rate constant (k_n) (Fig. 6(b)). The calculated k_n values for the studied alloys are tabulated in Table 3.

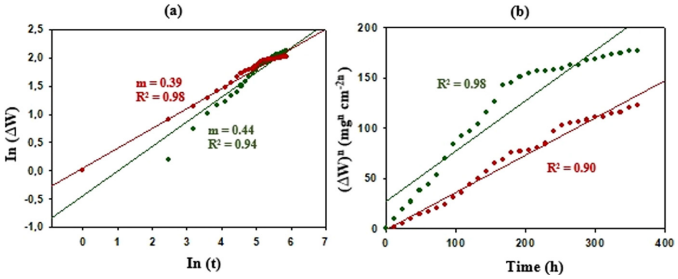

Fig. 6. (a) A double-logarithmic plot of weight change (ΔW) versus time (t), (b) the plot of oxidation rate constants (k_n) for the oxidized alloys. The green line and red line correspond to TiAlMo and TiAlNb alloys, respectively

TABLE 3

Possible equations and oxidation rate constants of alloys after oxidation at 900°C for 360 h

Alloy	ΔW (mg cm^{-2})	n	k_n (mg^n cm^{-2n} h^{-1})
TiAlMo	$y = 0.326\,x^{0.5682}$	2.27	0.3718
TiAlNb	$y = 1{,}129\,x^{0.3376}$	2.56	0.5010

It is worth noting that a lower value of oxidation rate constant would mean a smaller oxidation rate. The values of oxidation rate constant for oxidized TiAlMo and TiAlNb alloys at 900°C are 0.3718 and 0.5010 mg^n cm^{-2n} h^{-1}, respectively, showing that the oxidation resistance relatively improved with the addition Mo.

4.3. Phase composition of oxide scale

As can be seen in Fig. 7, after oxidation at 900°C for 360 h, the formed oxide scales on both alloys are made up of TiO_2 and Al_2O_3 oxides. The crystal structures of TiO_2 and Al_2O_3 phases are found to be rutile (JCPDS-ICDD card No: 21-1276) and corundum (JCPDS-ICDD No: 00-046-1212), respectively. Moreover, it is known that the corundum provides the best protection against high-temperature oxidation. However, one can see that the diffraction peaks of TiO_2 were more intensity compared to that of Al_2O_3. The matrix phases of TiAl and Ti_3Al were not found in the XRD analyses. The reason for this result is the thicker oxide scale formed on the alloys. Neither Mo-containing oxides nor Nb-containing oxides are detected in the

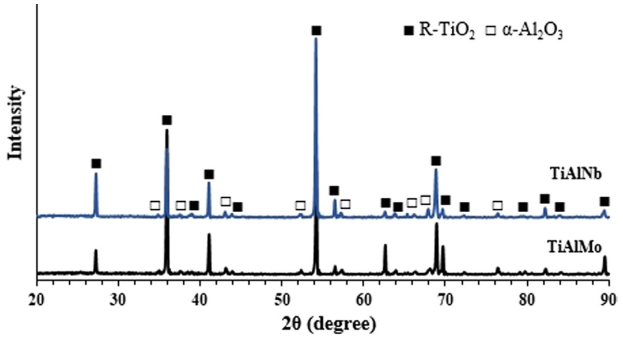

Fig. 7. XRD patterns of the alloys after oxidation at 900°C for 360 hours

oxide scales. The absence of Mo- and Nb-containing phases can be an indication of these metal atoms substitute Ti atoms in the TiO_2 lattice. This result is in good agreement with the report in Ref. [42].

However, the role played by the amount of the alloying element additions should be considered. This is because the defect structure of TiO_2 can be affected by the doping elements of different amounts.

4.4. Surface morphology and composition

Figure 8 shows the top-surface morphologies of the alloys oxidized at 900°C for 360 h. Table 4 is the corresponding chemical composition of the surface analyzed by EDS. Top surface SEM images show that the alloys' surface is covered with oxidation products, causing an undulant surface morphology. The higher magnification of marked regions display that the surface is mostly covered by irregularly oriented equiaxed oxide grains with polyhedron-shape. In addition, it can be noticed that the size of oxide grains developed on the TiAlNb was larger compared to that of TiAlMo. The average size of oxide grains for the TiAlMo and TiAlNb was about 2 µm and 3 µm, respectively. By considering the chemical composition corresponding to the points (1 and 2) in Fig. 11, it is reasonable to conclude that the oxide grains developed on the top surface were composed of TiO_2. This is also supported by the XRD patterns of the oxidized alloys in Fig. 7.

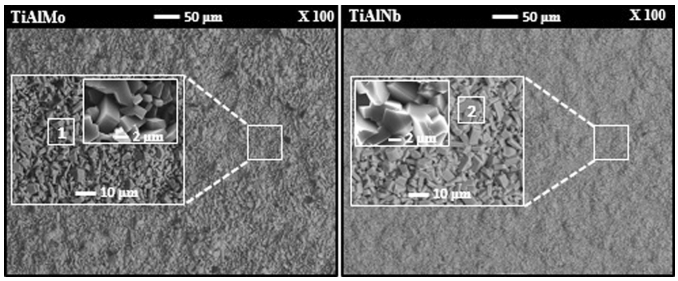

Fig. 8. Top surface SEM images of the alloys oxidized at 900°C for 360 h

TABLE 4

Chemical compositions (at.%) of points shown in Fig. 11

Point	Ti	Al	Mo	Nb	O
1	26.9	2.1	0.2	—	70.8
2	32.9	1.7	—	0,2	65.2

As can be noticed in EDS results, the content of Mo and Nb in the analyzed points was quite a few. This can be attributed to the fact that these elements are slow diffusers in TiAl alloys [4,8]. Besides, the lower amount of detected Al is derived from the underlying aluminum oxide layer. This implies that the outer TiO_2 layer is relatively thick. It is worth mentioning that the scale showed good adhesive property to the alloy surface and the scale of both alloys was not cracked, resulting in increased spallation resistance.

4.5. Cross-sectional analysis

After oxidation at 900°C for 360 h, TiAlMo and TiAlNb alloys were examined by SEM-EDS transverse section for the purpose of revealing the scale structure, composition and alloy-oxide interface. The cross-sectional SEM images of oxidized alloys are shown in Figure 9. Table 5 indicates the corresponding chemical composition of the points analyzed by EDS. As can be seen in Fig. 9, the oxide scales formed on the TiAlMo and TiAlNb alloys have a multilayered structure. Based on the EDS analysis results, the oxide scale structures of both alloys are found to be in the order of the inner mixture of TiO_2 and Al_2O_3 layer, transient Al_2O_3 layer and outer TiO_2 layer from the alloy-scale interface towards the surface. Such structure is characteristic for TiAl based alloys subjected to oxidation in air, and this phenomenon has been also observed by many researchers who have investigated the oxidation behavior of TiAl based alloys [2,4,12,13,43].

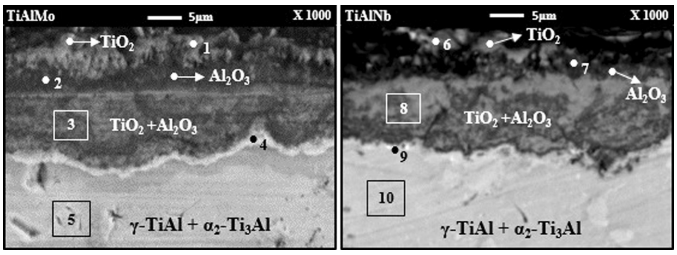

Fig. 9. Cross-section SEM image the alloys oxidized at 900°C for 360 h

TABLE 5

Chemical compositions (at.%) of points shown in Fig. 12

Point	Ti	Al	Mo	Nb	O
1	30.1	1.3	0.1	—	68.5
2	7.4	32.7	0.1	—	59.8
3	21.4	18.2	0.2	—	60.2
4	53.8	32.8	11.1	—	2.3
5	54.1	40.3	5.4	—	0.2
6	26.2	5.6	—	0.1	68.1
7	5.4	34.3	—	0.1	60.2
8	20.1	24.4	—	0.1	55.4
9	50.9	39.1	—	8.2	1.6
10	51.1	41.7	—	6.9	0.3

Mean thickness of the scale formed on TiAlMo and TiAlNb alloys was 20 µm and 17 µm, respectively. Regarding the oxidation process of TiAl alloys, it is important to note that the protective Al_2O_3 layer cannot form on top of the alloy since the chemical behavior of Ti and Al to oxygen are similar to each other [2,7,10]. Therefore, Al_2O_3 and TiO_2 form competitively at the same time during the first stage of oxidation [44]. The resulted TiO_2/Al_2O_3 mixture layer cannot retard the further oxidation of TiAl alloy, which is the reason why TiAl intermetallics exhibit weak oxidation resistance at elevated temperatures. It was reported that the Al_2O_3 layer can be generated on the outermost of the scale when the Al content exceeds at.% 50 [7]. However,

Ti-Al binary phase diagram shows that the two-phased TiAl alloy cannot be obtained when the Al content is over at.% 50. In addition, it is important to note that the oxidation resistance of the alloy increases with increasing Al content while its ductility decreases.

From the kinetic point of view, it is known that the growth velocity of Al_2O_3 is much lower compared to TiO_2 as the activation energy of Al_2O_3 is much higher than that of TiO_2 [10]. Accordingly, the chemical composition of points 1 and 6 in Table 5 show the presence of major amount of oxygen and titanium along with minor amount of aluminum and addition elements. By considering the EDS analysis (Table 5) in combination with XRD results (Fig.7), it is reasonable to conclude that these points corresponded to the TiO_2 phase. In the light of these considerations, one can see in Fig. 9 that the outermost layer of both alloys was covered by TiO_2 which has fast-growing kinetics. The growth of the outermost TiO_2 layer is taken place by the outward diffusion of Ti ions while oxygen ions diffused inward to form the inner mixed TiO_2/Al_2O_3 layer [45]. EDS analysis results of points 2 and 7 lying on the beneath of the outermost TiO_2 layer indicate the presence of an elevated amount of oxygen and aluminum along with minor amount of titanium and addition elements. This aluminum-rich oxide layer is generated due to the depletion of titanium, thereby promoting the possibility of Al_2O_3 formation. The obtained EDS results support the formation of alumina, which is consistent with the XRD analysis in Fig. 7. Beneath this Al_2O_3 layer, there is a mixture of TiO_2/Al_2O_3 layer (points 3 and 8), which forms the thickest part of the scale, in varying proportion. Therefore, it can be said that the thickness of oxide scale was controlled by mixed layer.

The TiO_2 generated on the TiAl surface is characterized as polyporous and non-stoichiometry n-type oxide. TiO_2 is flawed with oxygen vacancies which provide the fast diffusion channel for oxygen and thus it cannot protect against further oxidation [4,6,44]. It must be said that the main reason for the poor oxidation resistance of TiAl is due to the defect structure of TiO_2. However, Al_2O_3 plays an important role in preventing inward diffusion of oxygen due to a very low diffusivity of oxygen in alumina [42,46]. In other words, it can act as diffusion barriers and reduce the diffusion rate of species involved in the oxidation process. Consequently, oxygen is diffused preferentially by the oxygen vacancies in TiO_2.

Considering the role of addition alloying elements used in this study, it was explained on the basis of the fact that the oxygen vacancy concentration in the TiO_2 is decreased by the addition of alloying elements. When ions with higher valance electron higher than that of Ti^{4+}, for example Nb^{5+} or Mo^{6+}, are incorporated in the TiO_2, the substitution of these ions for Ti^{4+} in rutile lattice brings about in the annihilation of oxygen vacancies to compensate for excess positive charge results due to maintaining electroneutrality condition in the scale [4,6,42]. This allows us to conclude that the doping of Mo and Nb contributes to the reduction of TiO_2 growth rate and thus enhancement of oxidation resistance of TiAl. The addition of Mo causes the solubility of TiO_2 to decrease and this result gives rise to the outward growth of the oxide scale. Furthermore, protective alumina created during oxidation of Mo is defect-free and offers the superior oxidation resistance [46]. Shida and Anada [47] showed that the oxygen solubility in Ti-34.5Al (% 0.9) was higher compared to Ti-34.5Al-4Mo (% 0.55) and highlighted the effect of Mo that reduces internal oxidation of substrate.

In the case of Nb addition, the results obtained by Varma et al. [48] show that the weight change of Ti-44Al alloy significantly decreased by the addition of 4% Nb, whereas the additions of 8 and 11% Nb offer only a small further benefit. Additionally, it was reported the even 2% Nb addition to Ti-48Al-2Cr alloy plays a crucial role in the oxidation behavior of the alloy [49]. As it was mentioned before, critical Al concentration to form protective and continuous Al_2O_3 external layer on the TiAl surface is over at.% 50. Nb addition enhances the activity in favor of the Al (a_{Al}) in the alloy so that the compact alumina layer can be generated even when the Al content is less than at.% 50 [7,10].

It is worth noting that there are also sublayers (points 4 and 9) in Fig. 9 which are located between oxide scale and substrate. In these regions, the concentration of Mo and Nb is about 13 and 10 (at.%), respectively, as proved by the EDS analysis. The reason for this situation can be attributed to the ionic radius of Mo (0.65 Å) and Nb (0.69 Å) that have larger compared to Ti (0.60 Å) and Al (0.53 Å). On the other hand, the Nb and Mo addition elements are located in groups 5 and 6 of the periodic table, respectively. Taking the thermodynamic behaviors of these additions during oxidation into account, the Gibbs energy of formation of Nb_2O_5 and MoO_3 oxides for 1 mol of O_2 at 900°C is found approximately –556 and –304 kJ/mol, respectively. However, for the same conditions, the Gibbs energy of TiO_2 and Al_2O_3 formation is –732 and –869 kJ/mol, respectively. It can be seen that the latter oxides have higher thermodynamic stability. Accordingly, it is highly possible that the concentration of Nb and Mo is higher at the oxide scale/substrate interface.

4.6. NARX prediction model results

In the case of modeling the oxidation behavior of materials using ANN, not only saves the time required for experimental studies but also eliminates the various errors that may occur on a laboratory scale.

The NARX model with 2-20-10-2-2 structure used in this study was allowed to optimize the oxidation properties of the alloys based on input and output data. Fig. 10 shows that the structure used to involve 2 neurons in the input layer, 20 neurons in the first hidden layer, 10 neurons in the second hidden layer and 2 neurons in the output layer.

The trained network was then used to reveal between the experimental data and predicted data relation. Fig. 11 shows the comparison of the experimental data with the predicted data obtained using NARX model for TiAlMo and TiAlNb alloys after 360 h of oxidation at 900°C. It can be clearly seen that the predicted values are consistent with the ones obtained by experi-

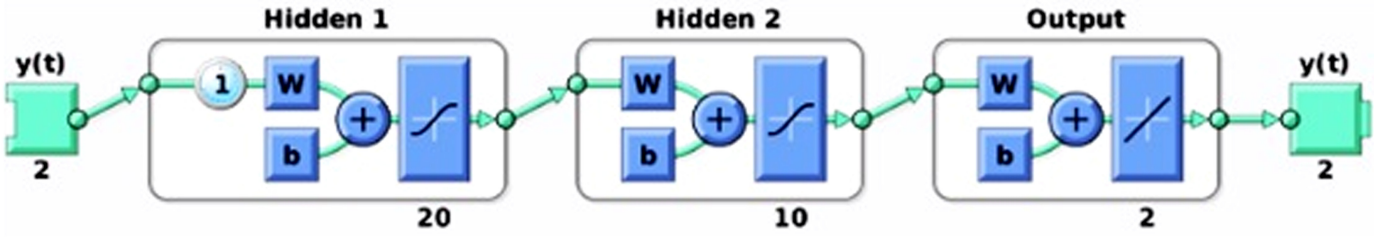

Fig. 10. NARX model in artificial neural network toolbox

mental study. As it was mentioned in the experimental part of this study, 80, 10 and 10 (in percentage,%) of total data were used to training data, testing data and validation data, respectively. The MSE% (mean squared error) values obtained for each alloy using Equation 2 and the results of NARX model training are listed in Table 6. The graphs of the NARX model training results were obtained but are not included in this study. According to Table 6, the MSE (%) values are small and the validation and the testing results also showed that the R values are very close to one, which indicates a good fit.

TABLE 6

The obtained NARX model results

Alloy	Data	Target Value	MSE (%)	R
TiAlMo	Training	25 (80%)	6.7815e-04	0.99998
	Validation	3 (10%)	0.4853	0.99941
	Testing	3 (10%)	0.6924	0.99906
TiAlNb	Training	25 (80%)	0.0012	0.99985
	Validation	3 (10%)	0.6343	0.99980
	Testing	3 (10%)	2.2258	0.99910

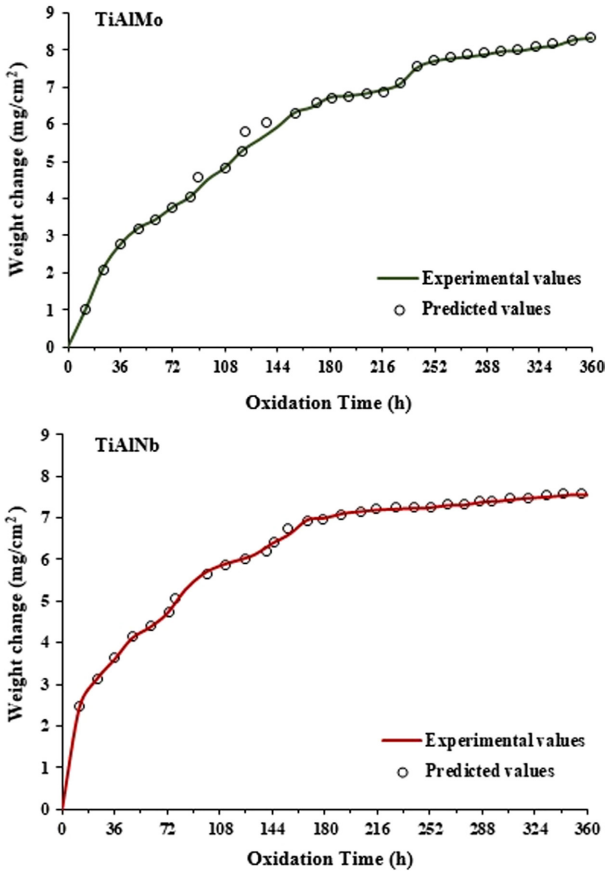

Fig. 11. Plots of comparison between predicted values with the experimental values for the oxidized alloys at 900°C

The analyses of the NARX neural network response were plotted in the form of linear regression analysis between the model predictions and the experimental results. Fig. 12 shows that a linear relationship is obtained between the predicted results and experimental results.

The obtained correlation coefficient (R) values are 0.9907 and 0.9923 for TiAlMo and TiAlNb alloys, respectively. This allows us to consider that the proposed NARX model presents a high degree of accuracy.

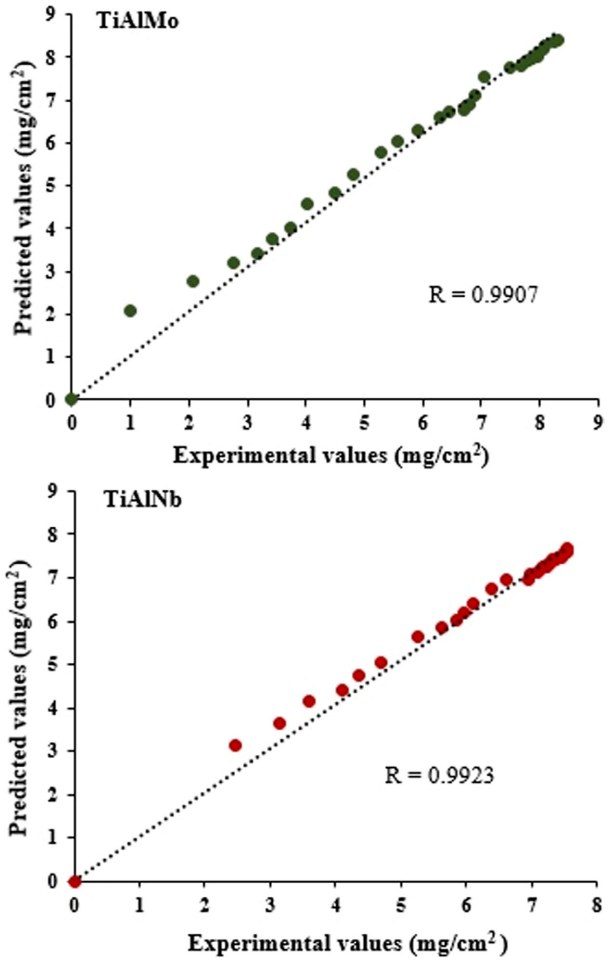

Fig. 12. The performance of NARX neural network for training values, comparing the model prediction and experimental results

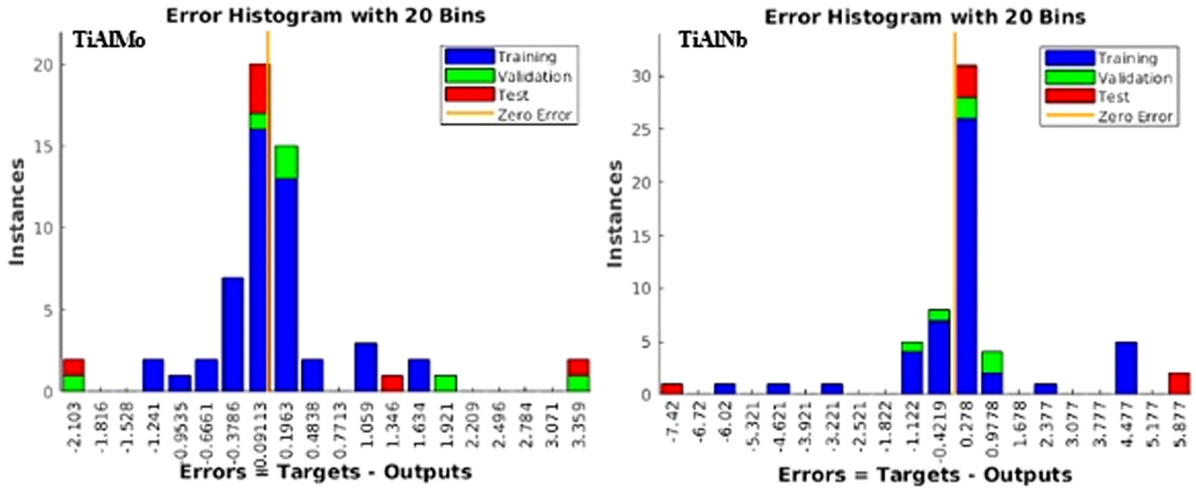

Fig. 13. Error histogram of the NARX prediction model for TiAlMo and TiAlNb alloys

An error histogram analysis was performed to further confirm the performance of the NARX neural network. The resulted plot (Fig. 13) is a representation of how error sizes are distributed. For the involved data set, the error of NARX model prediction was found to be within ±3%. Based on the obtained result, it can be said that a high degree of reliance on the accuracy of the NARX model.

5. Conclusions

In the present study, the cyclic oxidation behavior of at.% Ti-44Al-3Mo and Ti-44Al-3Nb alloys sintered by electrical resistance sintering (ERS) technique was investigated at 900°C for 360 h. After 360 h of oxidation at 900°C, the occurred weight changes on the alloys were predicted using a nonlinear autoregressive neural network (NARX). According to the results obtained from this study, the following conclusions can be made:

1. ERS sintered Ti-44Al-3Mo and Ti-44Al-3Nb (at.%) alloys are composed of γ-TiAl and α_2-Ti_3Al phases, as purposed.
2. After being oxidized at 900°C for 360 h, the total weight change of TiAlMo and TiAlNb alloys was approx. 8.3 and 7.55 mg/cm^2, respectively.
3. Oxidation kinetics of the TiAlMo obeys a nearly parabolic relationship, while that of the TiAlNb follows a rate law intermediate between parabolic and cubic relationship.
4. The oxidation products are composed of TiO_2 and Al_2O_3 oxides for both alloys. The oxide scale structure of alloys consisted of the following consecutive layers starting from the substrate: TiO_2+Al_2O_3/Al_2O_3/TiO_2. Moreover, both oxide scales have a good adherent relationship with the substrate.
5. NARX model findings showed that weight change data can be effectively used for modelling and prediction. The model predictions were compared to the corresponding experimental results and found that there is a linear relationship. The correlation coefficient (R) values are 0.9907 and 0.9923 for TiAlMo and TiAlNb, respectively. This is an indication that the model used has a high performance in the prediction of the oxidation behavior of the alloys.

REFERENCES

[1] J. Jiang, Y. Hea, C.T. Liu, Intermetallics **93**, 217-226 (2018). http://dx.doi.org/10.1016/j.intermet.2017.06.003

[2] M. Bik, A. Gil, M. Stygar, J. Dąbrowa, P. Jeleń, E. Długoń, M. Leśniak , M. Sitarz, Intermetallics **105**, 29-38 (2019). https://doi.org/10.1016/j.intermet.2018.09.014

[3] P. V. Cobbinah, W.R. Matizamhuka, R. Machaka, M.B. Shongwe, Y. Y-Mitarai, Int. J. Adv. Manuf. Tech. **106**, 3203-3215 (2020). https://doi.org/10.1007/s00170-019-04885-7

[4] Y. Garip, O. Ozdemir, J. Alloy Compd. **818**, 152818 (2020). https://doi.org/10.1016/j.jallcom.2019.152818

[5] Y. Garip, O. Ozdemir, J. Alloy Compd. **780,** 364-377 (2019). https://doi.org/10.1016/j.jallcom.2018.11.324

[6] P.V. Cobbinah, W.R. Matizamhuka, Adv. Mater. Sci. Eng. 1-21 (2019). https://doi.org/10.1155/2019/4251953

[7] I.C. Alagić , Z. Cvijović, D. Zagorac, M.T. Jovanović, Ceram. Int. **45** (7), Part B, 9423-9438 (2019). https://doi.org/10.1016/j.ceramint.2018.08.287

[8] M. Mitoraj, E.M. Godlewska, Intermetallics **34**, 112-121 (2013). http://dx.doi.org/10.1016/j.intermet.2012.10.014

[9] A. Choudhury, M. Blum, Vacuum **47**, 829-831 (1996). https://doi.org/10.1016/0042-207X(96)00076-0.

[10] J. Dai, J. Zhu, C. Chen, F. Weng, J. Alloy Compd. **68**, 784-798 (2016). http://dx.doi.org/10.1016/j.jallcom.2016.06.212

[11] M.N. Mathabathea, A.S. Bolokang, G. Govender, R.J. Mostert, C.W. Siyasiya, Vacuum **154**, 82-89 (2018). https://doi.org/10.1016/j.vacuum.2018.04.055

[12] J. Małecka, W. Grzesik, A. Hernas, Corros. Sci. **52**, 263-272 (2010). https://doi.org/10.1016/j.corsci.2009.09.015

[13] D.J. Kim, D.Y. Seo, H. Saari, T. Sawatzky, Y.W. Kim, Intermetallics **19**, 1509-1516 (2011). https://doi.org/10.1016/j.intermet.2011.05.027

[14] D. Pilone, F. Felli, Intermetallics **26**, 36-39 (2012). https://doi.org/10.1016/j.intermet.2012.03.008

[15] A. Brotzu, F. Felli, D. Pilone, Intermetallics **54**, 176-180 (2014). http://dx.doi.org/10.1016/j.intermet.2014.06.007

[16] T. Popela, D. Vojtech, J.-B. Vogt, A. Michalcová, Appl. Surf. Sci. **307**, 579-588 (2014). http://dx.doi.org/10.1016/j.apsusc.2014.04.076

[17] O.F. Ogunbiyi, T. Jamiru, E.R. Sadiku, L.W. Beneke1, O.T. Adesina, T.A. Adegbola, Int. J. Adv. Manuf. Tech. **104**, 1425-1436 (2019). https://doi.org/10.1007/s00170-019-03983-w

[18] J.M. Montes, F.G. Cuevas, F. Ternero, R. Astacio, E.S. Caballero, J. Cintas, Metals (**8**) 426, 1-14 (2018). https://doi.org/10.3390/met8060426

[19] P. Jajarmi, S. Valipour, Comp. Mater. Sci. **47**, 106-110 (2009). https://doi.org/10.1016/j.commatsci.2009.06.017

[20] J. McBride, S. Malinov, W. Sha, Mater. Sci. Eng. A **384,** 129-137 (2004). https://doi.org/10.1016/j.msea.2004.05.072

[21] D.W. Yun, S.M. Seo, H.W. Jeong, I.S. Kim, Y.S. Yoo, J. Alloy Compd. **587**, 105-112 (2014). http://dx.doi.org/10.1016/j.jallcom.2013.10.138

[22] I. Kucuk, T. Yildirim, N.M. Gasanly, H. Ozkan, J. Alloy Compd. **507**, 517-520 (2010). https://doi.org/10.1016/j.jallcom.2010.08.009

[23] T. Dudziaka, P. Gajewskib, B. Śnieżyńskib, V. Deodeshmukhc, M. Witkowskad, W. Ratuszek, K. Chruściel, Corros. Sci. **133**, 94-111 (2018). https://doi.org/10.1016/j.corsci.2018.01.013.

[24] S. Danaher, T. Dudziak, P.K. Datta, R. Hasan, P.S. Leung, Corros. Sci. **69**, 322-337 (2013). http://dx.doi.org/10.1016/j.corsci.2012.12.016

[25] K. Dehghani, A. Nekahi, Mater. Design **31**, 2224-2229 (2010). https://doi.org/10.1016/j.matdes.2009.10.020

[26] S.H. Mousavi Anijdan, A. Bahrami, H.R. Madaah Hosseini, A. Shafyei, Mater. Design **27**, 605-609 (2006). https://doi.org/10.1016/j.matdes.2004.11.027

[27] A. Bahrami, S.H. Mousavi Anijdan, A. Ekrami, J. Alloy Compd. 3**92**, 177-182 (2005). https://doi.org/10.1016/j.jallcom.2004.09.014

[28] S. Guessasma, C. Coddet, Acta Mater. **52**, 5157-5164 (2004). https://doi.org/10.1016/j.actamat.2004.07.022

[29] A.R. Carvalho, F.M. Ramos, A.A. Chaves, Neural. Comput. Appl. 2**0**, 1273-1284 (2011). https://doi.org/10.1007/s00521-010-0504-3

[30] A.M. Rashidi, M. Hayati, A. Rezaei, Mater. Design **42**, 308-316 (2012). http://dx.doi.org/10.1016/j.matdes.2012.06.011

[31] M. Yetkin, Y. Kim, Appl. Ocean. Res. **88**, 170-186 (2019). https://doi.org/10.1016/j.apor.2019.04.013

[32] R. Matkovskyy,T. Bouraoui, J. Quant. Econ. **17**, 433-446 (2019). https://doi.org/10.1007/s40953-018-01338

[33] Y. Garip, Sakarya University, Doctoral Thesis (2019).

[34] K. Kothari, R. Radhakrishnan, N.M. Wereley, Prog. Aerosp. Sci. **55**, 1-16 (2012). http://dx.doi.org/10.1016/j.paerosci.2012.04.001

[35] M.A. Lagos, I. Agote, Intermetallics **36**, 51-56 (2013). http://dx.doi.org/10.1016/j.intermet.2013.01.006

[36] J.B. Yang, W.S. Hwang, JMEPEG **7** (3), 385-392 (1998). https://doi.org/10.1361/105994998770347837

[37] O. Ostrovskaya, C. Badini, G. Baudana, E. Padovano, S. Biamino, Intermetallics **93**, 244-250 (2018). http://dx.doi.org/10.1016/j.intermet.2017.09.020

[38] H. Anada, Y. Shida, Mater. Trans. **36** (4):533-539 (1995). https://doi.org/10.2320/jinstmet1952.58.7_746

[39] L. Chena, H. Lan, C. Huang, B. Yanga, L. Du, W. Zhang, Eng. Fail. Anal. **79**, 245-252 (2017). http://dx.doi.org/10.1016/j.engfailanal.2017.05.009

[40] J.W. Fergus, Mater. Sci. Eng. A **338**, 108-125 (2002). https://doi.org/10.1016/S0921-5093(02)00064-3

[41] H. Guleryuz, H. Cimenoglu, J. Alloy Compd. **472**, 241-246 (2009). https://doi.org/10.1016/j.jallcom.2008.04.024

[42] D. Vojtech, T. Popela, J. Kubásek, J. Maixner, P. Novák, Intermetallics **19**, 493-501 (2011). https://doi.org/10.1016/j.intermet.2010.11.025

[43] P. Ouyang, G. Mi, P. Li, L. He, J. Cao, X. Huang, Materials **12**, 2114, 1-21 (2019). https://doi.org/10.3390/ma12132114

[44] F.P. Ping, Q. M. Hu, A. V. Bakulin, S.E. Kulkova, R. Yang, Intermetallics **68**, 57-62 (2016). https://doi.org/10.1016/j.intermet.2015.09.005

[45] X. Liu, K. You, Z. Wang, M. Zhang, Z. He, Vacuum **89**, 209-214 (2013). https://doi.org/10.1016/j.vacuum.2012.05.015

[46] M. Naveed, A.F. Renteria, S. Weiß, J .Alloy Comp. **691**, 489-497 (2017). https://doi.org/10.1016/j.jallcom.2016.08.259

[47] Y. Shida, H. Anada, Mater. Trans. JIM, **35** (9), 623-631 (1994). https://doi.org/10.2320/matertrans1989.35.623

[48] S.K. Varma, A. Chan, R.N. Mahapatra, Oxid. Met. **55**, 423-435 (2001). https://doi.org/10.1023/A:101035161

[49] V.A.C. Haanappel, J.D. Sunderkotter, M.F. Stroosnijder, Intermetallics **7**, 529-541 (1999). https://doi.org/10.1016/S0966-9795(98)000764